

THE SENSITIVITY OF CORE-COLLAPSE SUPERNOVAE TO NUCLEAR ELECTRON CAPTURE

CHRIS SULLIVAN^{1,2,3†}, EVAN O’CONNOR^{4,5‡}, REMCO G. T. ZEGERS^{1,2,3}, THOMAS GRUBB^{1,2,3}, SAM M. AUSTIN^{1,2,3}

¹National Superconducting Cyclotron Laboratory, Michigan State University, East Lansing, MI 48824, USA

²Department of Physics and Astronomy, Michigan State University, East Lansing, MI 48824, USA

³Joint Institute for Nuclear Astrophysics: CEE, Michigan State University, East Lansing, MI 48824, USA

⁴North Carolina State University, Department of Physics, Campus Code 8202, Raleigh, NC 27695, USA and

⁵CITA, Canadian Institute for Theoretical Astrophysics, Toronto, Canada, M5S 3H8

(Dated: July 1, 2021)

Draft version July 1, 2021

Abstract

A weak-rate library aimed at investigating the sensitivity of astrophysical environments to variations of electron-capture rates on medium-heavy nuclei has been developed. With this library, the sensitivity of the core-collapse and early post-bounce phases of core-collapse supernovae to nuclear electron-capture is examined by systematically and statistically varying electron-capture rates of individual nuclei. The rates are adjusted by factors consistent with uncertainties indicated by comparing theoretical rates to those deduced from charge-exchange and β -decay measurements. To ensure a model independent assessment, sensitivity studies across a comprehensive set of progenitors and equations of state are performed. In our systematic study, we find a +16/-4% range in the mass of the inner-core at the time of shock formation and a $\pm 20\%$ range of peak ν_e -luminosity during the deleptonization burst. These ranges are each five times as large as those seen from a separate progenitor study in which we evaluated the sensitivity of these parameters to 32 presupernova stellar models. It is also found that the simulations are more sensitive to a reduction in the electron-capture rates than an enhancement, and in particular to the reduction in the rates for neutron-rich nuclei near the $N = 50$ closed neutron-shell. As measurements for medium-heavy ($A > 65$) and neutron-rich nuclei are sparse, and because accurate theoretical models which account for nuclear structure considerations on the individual nucleus level are not readily available, rates for these nuclei may be overestimated. If more accurate estimates confirm this, results from this study indicate that significant changes to the core-collapse trajectory can be expected. For this reason, experimental and theoretical efforts should focus in this region of the nuclear chart.

1. INTRODUCTION

The study of interactions mediated via the weak nuclear force is of importance to a large number of fields in physics. However, it is of particular importance to the field of astrophysics because of the longer timescale on which weak interactions operate as compared to the strong and electromagnetic interactions. This is evidenced by the impact that new insights into weak reaction physics have on astrophysical models (Langanke & Martínez-Pinedo 2003). Specifically, electron-capture reactions play a prominent role in high-density environments such as those found in the late stages of massive star evolution (Heger et al. 2001; Martínez-Pinedo et al. 2014), thermonuclear (Iwamoto et al. 1999; Brachwitz et al. 2000) and core-collapse supernovae (CCSNe) (Hix et al. 2003; Janka et al. 2007), neutron stars (Gupta et al. 2007; Schatz et al. 2014), and compact object merger events (Goriely et al. 2015). Realistic simulations of these environments rely on accurate nuclear physics inputs including electron-capture rates.

Electron-capture rates depend sensitively on Gamow-Teller (GT) transition-strength distributions in the β^+ direction. These transition strengths characterize nuclear excitations in which a single unit of spin and isospin are transferred ($\Delta S, \Delta T = 1$), with no transfer of orbital angular momentum ($\Delta L = 0$). While the main component of electron capture occurs on the ground state configuration of a nucleus, in high temperature stellar environments electron captures on thermally-populated excited states of the parent nucleus can also contribute significantly to the overall rate (Langanke & Martínez-

Pinedo 2000). Unfortunately, it is difficult to obtain information about transitions from excited states in the laboratory. Compounding the problem is the fact that in order to accurately include electron capture in simulations one must include electron captures on a wide range of nuclei. Hence, in general one must rely on theoretical models for a complete description of stellar electron-capture rates. On the other hand, measurements of Gamow-Teller strength distributions in a representative set of nuclei are important for the development and benchmarking of robust theories. At the same time, it is critical that theoretical and computational efforts provide guidance to experimenters on which measurements to perform.

Presently, configuration-interaction (shell-model) calculations are the primary method for producing reliable GT strength distributions near stability in the sd - and pf -shells ($8 < [N, Z] < 20$ and $20 < [N, Z] < 40$, respectively) for electron capture on both ground and excited states (Oda et al. 1994; Langanke et al. 2003). Quasi-particle random-phase approximation (QRPA) calculations have also been utilized to estimate GT strengths for large sets of nuclei, but only where transitions from the ground state are considered (Paar et al. 2009; Möller & Randrup 1990; Dzhioev et al. 2010; Niu et al. 2011; Nabi & Klapdor-Kleingrothaus 2004). Furthermore, comprehensive sets of electron-capture rates (as a function of density and temperature) for a large number of nuclei based on QRPA calculations have not been published.

Direct and indirect experiments, such as β -decay and charge-exchange (CE) measurements respectively, pro-

[†]sullivan@nscl.msu.edu

[‡] Hubble Fellow

vide robust benchmarks for theoretical GT strengths and therefore are crucial for our understanding of astrophysical electron-capture rates. Unfortunately, electron-capture and β -decay experiments can only access states in a limited Q-value window. Furthermore, for neutron-rich nuclei β -decay only provides information in the β^- direction, which is of limited use for electron-capture studies. Intermediate energy ($\gtrsim 100$ MeV/u) CE reactions in the β^+ direction, however, connect the same initial and final states as electron capture, providing information about transitions up to high excitation energies, and are thus well suited to study the full Gamow-Teller strength distribution of interest. At these energies, CE measurements are accurate at the $\sim 10\%$ level and are therefore able to provide rigorous tests of theoretical Gamow-Teller strengths and derived electron-capture rates.

Recently, the results from (n,p), ($d,^2\text{He}$), and ($t,^3\text{He}$) CE reactions on nuclei in the pf -shell were systematically compared (Cole et al. 2012; Scott et al. 2014; Noji et al. 2014) with shell-model calculations using the KB3G (Poves et al. 2001) and GXPF1a (Honma et al. 2005) effective interactions in the pf -model space, and with calculations based on the QRPA formalism of Möller & Randrup (1990). The authors compared shell-model and QRPA derived electron-capture rates against those derived from CE measurements. It was found that the QRPA calculations systematically overestimate the electron-capture rates (~ 100 -3000%, depending on density and temperature), whereas the shell-model estimates produce rates similar to those measured experimentally (~ 1 -50%) (Cole et al. 2012). Unfortunately, shell-model calculations are computationally challenging for nuclei beyond the pf -shell, and therefore weak rates used in high-density astrophysical calculations most commonly rely on less accurate methods. In each of these cases, systematic and random error exist, and it is therefore important to understand the sensitivity of astrophysical simulations to uncertainties in these rates.

Sensitivity studies are useful tools for guiding theoretical and experimental efforts because they highlight nuclei that should be given particular focus, and they indicate the accuracy with which the parameters of interest need to be known. They also illustrate how strongly the current parameter uncertainties affect the outcome of the astrophysical simulations. In this work, we perform ~ 150 collapse simulations examining how systematic and statistical variations of the electron-capture rates impact the collapse, bounce and pre-explosion phases of core-collapse supernovae simulations over a range of presupernova progenitors and equations of state (EOS). We describe the development of a modular and open-source weak reaction rate library for use in astrophysical simulations and its first implementation using the stellar core-collapse code GR1D (O’Connor & Ott 2010). In the following sections, we show that the inner core of the proton-neutron star (PNS) and the observable peak neutrino-luminosity from core bounce and shock formation depend sensitively ($+16/-4\%$ and $\pm 20\%$, respectively) on the electron-capture rates of neutron-rich nuclei. As variations on this level are not easily reproduced from uncertainties in other inputs to the simulations, they motivate the development of new theoretical models for electron-capture rates as well as relevant measurements, which together will constrain these and other key parameters discussed in this work.

In Section 2 we discuss previous development of weak rates for astrophysics, as well as the implementations made in this work. In Section 3 we motivate the importance of electron-capture rates during the core-collapse phase of CCSNe, and in Section 4 we describe the codes we have utilized and developed for this work. We detail the sensitivity studies performed in Section 5 and conclude in Section 6.

2. ASTROPHYSICAL WEAK INTERACTION RATES

From the birth to the death of massive stars, the weak nuclear force is a primary actor in the story of stellar evolution (Langanke & Martínez-Pinedo 2003). Weak interactions are important ingredients for nucleosynthesis and also for the internal structure of evolving stars, as they sensitively determine the electron-to-baryon ratio Y_e and the iron-core mass just prior to core-collapse (Heger et al. 2001). Unlike the conditions present during quasistatic stellar evolution, however, in the core of a collapsing star the density and temperature are high enough that nuclear and electromagnetic reactions equilibrate (Iliadis 2007). Weak reactions, on the other hand, operate much more slowly and thus continue to affect the nuclear composition, the neutrino emission, and ultimately the dynamics of the entire event.

As compared to other semi-leptonic weak interactions, electron capture has a particularly remarkable impact on the core-collapse environment (Langanke & Martínez-Pinedo 2014). In the final stages of a star’s life, the nuclear-energy generation rate of the core that normally sustains a star against gravitational collapse is absent because the core is composed of highly stable iron peak nuclei. Instead, at these late times the electron-degeneracy pressure provides the primary stability against collapse. It is therefore apparent that electron captures that remove electrons from the system will have dramatic consequences for this environment. Furthermore, the electron chemical potential μ_e is sufficiently large to overcome Q-value restrictions, and so the electron-capture rates are significant.

Just prior to and during the early moments of collapse, other weak interactions can also play a role. Martínez-Pinedo et al. (2000) have shown that β^- -decay can temporarily compete with electron capture when $Y_e=0.42$ -0.46, which can occur during Si shell burning and the early stages of collapse. However, as collapse ensues, μ_e quickly becomes large enough that β -decay electrons are energetically blocked due to degeneracy. Similarly, β^+ -decay can also compete with electron-capture for nuclei with $Q_{e^+} > 2m_e c^2$, but in the core-collapse environment neutron-rich conditions are favored, and Q_{e^+} is below this threshold.

The importance of reactions mediated by the weak nuclear force, and specifically electron capture, as it pertains to core-collapse was first demonstrated by Bethe et al. (1979). Not long after, the theory of stellar electron capture was formalized by Fuller, Fowler, and Newman (FFN) (Fuller et al. 1982). In their pioneering work they published the first tabulation of weak interaction rates (β^\pm -decay and e^\pm -capture) considering presupernova conditions where allowed Fermi and Gamow-Teller (GT) transitions dominate. Since then, advancements in computational resources have allowed for detailed nuclear shell-model calculations that have increased the accuracy

of the weak-interaction theory first outlined by FFN. Major weak-interaction rate tabulations that derive from a combination of experimental data and shell-model effective interactions are the Oda et al. (1994) and Langanke & Martínez-Pinedo (2000) tabulations for *sd*- ($A=17-39$) and *pf*-shell ($A=45-65$) nuclei respectively. For heavier nuclei, the Shell Model Monte Carlo (SMMC) approach has been employed to preserve nuclear properties such as the correlation energy scale in very large model spaces (Langanke et al. 2003). Langanke et al. (2003) have combined this method with an RPA technique to estimate electron-capture rates at densities and temperatures relevant during core-collapse for nuclei in the *pf*/*sdg*-shell ($A=65-112$), which have come to be known as the LMSH rates. Juodagalvis et al. (2010) have also produced a set of more than 2200 additional rates based on the same RPA technique but utilizing a Fermi–Dirac parameterization instead of the more computationally expensive SMMC calculations. The individual rates were not released, but instead these rates were averaged over NSE abundances and reported along a characteristic core-collapse (ρ, T, Y_e) trajectory. Unfortunately, this is not suitable for the present study in which we investigate the detailed sensitivity on a nucleus by nucleus basis.

In this work, we have implemented each of the rate tabulations listed in Table 1, which together contain 445 rates for 304 unique nuclei over a large density and temperature grid. This library has been built as a standalone module and has also been implemented into the neutrino-interaction library NuLib (O’Connor 2015) for use in neutrino-transport routines employed by the spherically-symmetric, general-relativistic stellar collapse code GR1D (O’Connor 2015)—see Section 4 for more information. Details on the density and temperature range for each of the included rate tabulations are shown in Table 1. The mass coverage of each rate table is shown in Figure 1.

The LMP+LMSH rates were first implemented into a spherically-symmetric core-collapse simulation by Hix et al. (2003). They compared simulations with this set of shell-model based electron-capture rates against simulations that utilized the Bruenn (1985) prescription for electron capture. The evolution of the core-collapse phase and the structural differences in the core at bounce seen in that work were significant. In light of the differences that exist between theoretical estimates for electron-capture rates and those inferred from CE experiments, these results motivate the need for a detailed sensitivity study.

To handle the large number of nuclei not included in the tables, Hix et al. (2003) utilized an average electron-capture neutrino emissivity for all nuclei which lacked a shell-model based rate. Here, instead of performing averaging, we employ the approximate routine of Langanke et al. (2003), which is based on the parameterization of the electron-capture rate as a function of the ground state to ground state Q-value. This approximation was first described by Fuller et al. (1985) and was later parameterized and fit to shell-model calculations in the *pf*-shell by Langanke et al. (2003). In this approximation, the electron-capture rate is written as:

$$\lambda_{\text{EC}} = \frac{\ln 2 \cdot B}{K} \left(\frac{T}{m_e c^2} \right)^5 [F_4(\eta) - 2\chi F_3(\eta) + \chi^2 F_2(\eta)] \quad (1)$$

and the neutrino-energy loss rate is,

$$\lambda_{\nu_e} = \frac{\ln 2 \cdot B}{K} \left(\frac{T}{m_e c^2} \right)^6 [F_5(\eta) - 2\chi F_4(\eta) + \chi^2 F_3(\eta)], \quad (2)$$

where m_e is the electron mass, $K = 6146 \text{ s}$, F_k are Fermi integrals of rank k and degeneracy η , $\chi = (Q - \Delta E)/T$, $\eta = \chi + \mu_e/T$, and T and μ_e are the temperature and electron chemical potential. B ($= 4.6$) and ΔE ($= 2.5 \text{ MeV}$) are fit parameters taken from Langanke et al. (2003) and respectively represent effective values for the transition strength and energy difference between final and initial excited states.

In Figure 2 we compare the rate estimates from this approximation and those from the tables. As is easily seen from the figure, the variance of the shell-model rates depends sensitively on the density of the environment. At lower densities, where the electron chemical-potential and electron capture Q-value are comparable ($\mu_e \approx Q_{\text{EC}}$), the location of excited states in the daughter nucleus, and the associated Gamow-Teller transition strength, sensitively determine the total electron-capture rate for a nucleus. New final states in the daughter nucleus become accessible as the electron Fermi-energy, which scales with μ_e , increases beyond the energy required to populate them via allowed electron capture. The large scatter of the electron-capture rates at lower densities (Fig. 2) is because the Fermi energy is comparable to the excited state energies of the daughter nuclei and the internal structure of each nucleus varies significantly. During collapse, as the density increases and the material becomes more neutron rich due to successive electron captures, both the magnitude of the average electron capture Q-value and μ_e increase. However, μ_e increases more quickly with density than the reaction Q-values do, and eventually $\mu_e \gg Q_{\text{EC}}$ implying that the majority of the electron-capture channels are open. In this regime the rate is less sensitive to the excitation energy spectrum of the daughter nucleus, and instead depends more strongly on the total GT strength across all possible final states. The decrease in the variance of the shell-model electron-capture rates in the higher density case of Figure 2 is a result of this.

While the parameters of Eqs. 1 and 2 were originally fit from the LMP nuclei, there is reasonable agreement of the approximation with the other tabulated rates. Outside of these tables, significant deviations from the estimates of this approximation may exist, specifically for heavier neutron rich nuclei (Juodagalvis et al. 2008). But for the purpose of a sensitivity study, this approximation—from which the majority of the rates are calculated—is used as a base estimate off which the electron-capture rates may be varied. In Section 5.2 we show, given this set of rates, that heavier neutron-rich nuclei are the most important in the simulations. However, electron-capture rates developed from sophisticated theoretical models do not exist for individual nuclei in this region, and thus cannot be benchmarked against experimental measurements.

TABLE 1
DENSITY, TEMPERATURE AND MASS RANGES FOR THE COMPILED WEAK RATE SET

Model space							Ref.	
Table	s	p	sd	pf	$pf g/sdg$	T (GK)		$\text{Log}_{10}(\rho Y_e \text{ g cm}^{-3})$
FFN	x		x	x		0.01 - 100	1.0 - 11	Fuller et al. (1982)
ODA	x		x			0.01 - 30	1.0 - 11	Oda et al. (1994)
LMP	x			x		0.01 - 100	1.0 - 11	Langanke et al. (2003)
LMSH					x	8.12 - 39.1	9.22 - 12.4	Hix et al. (2003); Langanke et al. (2001a)
Approx.	x	x	x	x	x	-	-	Langanke et al. (2003)

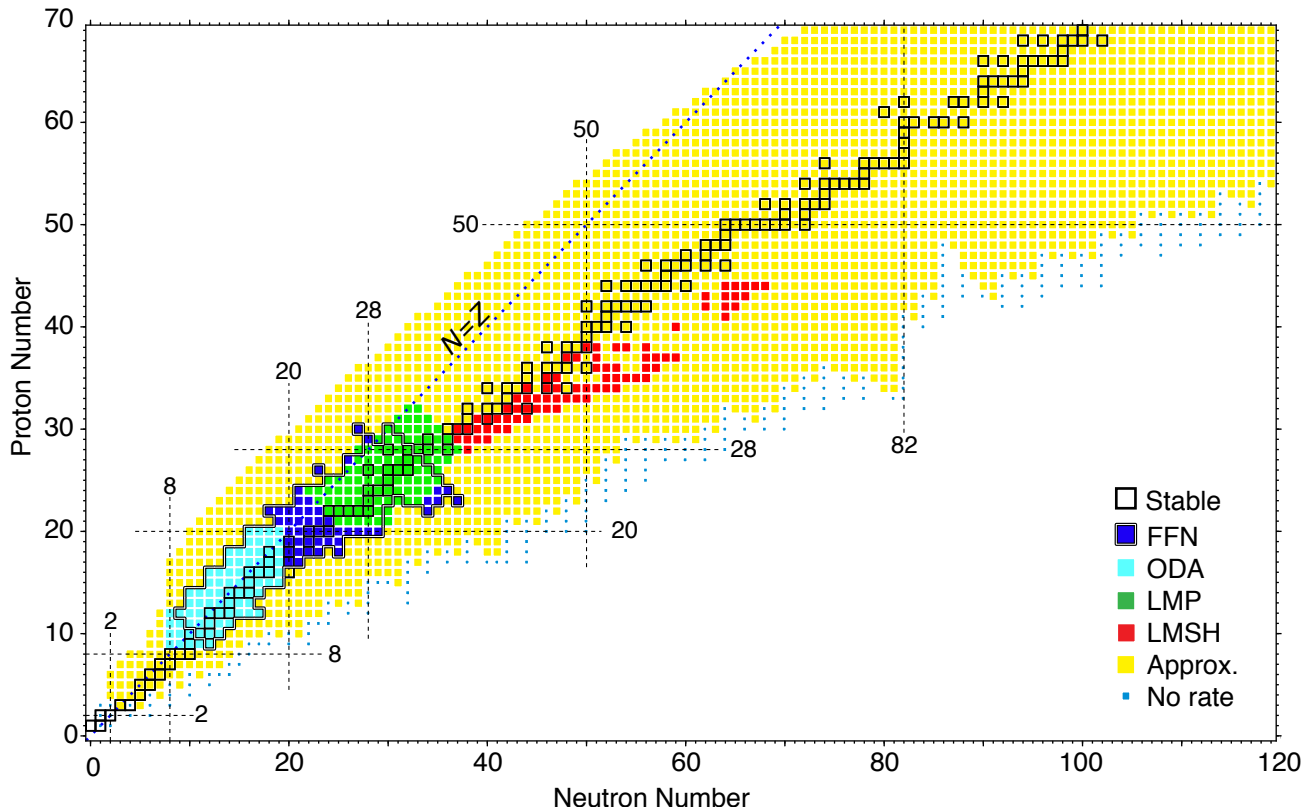


FIG. 1.— Chart of the nuclear species included in each weak rate table. The table to which a species belongs is given by the color and legend in the figure. The Oda set contains rates for lower mass sd -shell nuclei (light blue), the LMP set contains rates for the intermediate mass pf -shell nuclei (green), and the LMSH set contains rates for the heavier mass $pf g/sdg$ -shell nuclei near stability (red). The FFN tabulation provides rates across the sd and pf -shells (dark blue). Squares individually bordered in black are stable nuclei. The tables are mutually exclusive except for FFN which spans many nuclear shells. To distinguish between nuclei with rates from FFN and another table, the border of the FFN set has been outlined with a black and white line.

Therefore, the estimates provided by the approximation of Eqs. 1 and 2 may be systematically off by a considerable amount. As we will show, changes in the predicted rates for these nuclei have significant consequences for the simulations, motivating the need for experimental and theoretical efforts to constrain the rates of these species.

3. CORE COLLAPSE AND THE ROLE OF ELECTRON CAPTURE

Just prior to collapse, the temperature of the stellar core becomes high enough ($T \gtrsim 0.5$ MeV) that the photon gas has sufficient energy to photodissociate nuclei into alpha particles and free nucleons. However, the density is also high ($\rho \gtrsim 10^9 \text{ g cm}^{-3}$) resulting in large nuclear reaction rates that rapidly form nuclei from these light particles. The balance reached between these competing processes is known as Nuclear Statistical Equilibrium (NSE). If the

entropy is sufficiently low and the mass fraction of free nucleons is small compared to that of nuclei, the most abundant nucleus in NSE is the species with the highest binding energy for a given electron-fraction, $Y_e (= Z/A)$ (Martínez-Pinedo et al. 2000). A broad distribution of abundant nuclei forms due to finite temperatures which distribute the abundances around these peak nuclei.

As collapse ensues and the central density increases through the first few decades, electron captures are the primary engine of deleptonization. Electrons are removed from the system and the produced electron-neutrinos (ν_e) are able to freely stream out of the core, decreasing both Y_e and total lepton fraction Y_l . As Y_e decreases, peak abundances move toward neutron-rich nuclei, and the core begins to cool as ν_e 's carry away energy and entropy. Electron captures continue to dominate the neutrino transport during collapse until the last few mil-

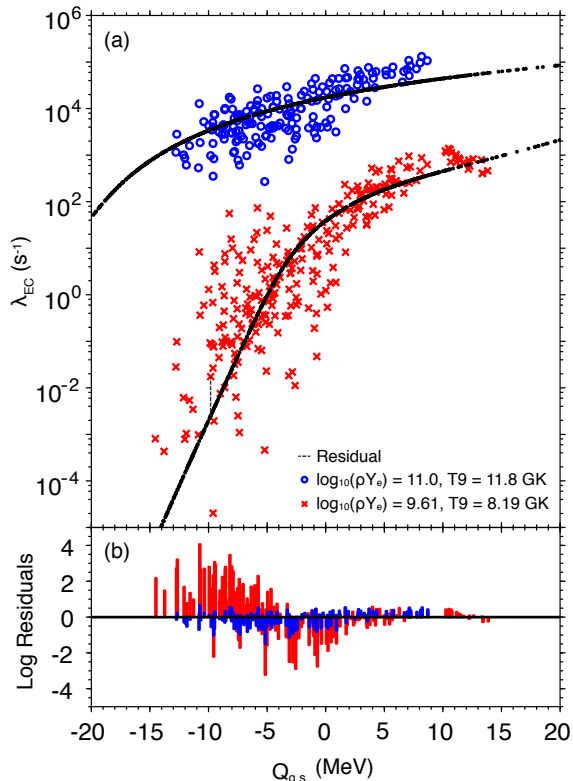


FIG. 2.— Panel (a): Q -value dependence of electron-capture rates at two points along a core-collapse trajectory. The scattered points are tabulated (shell-model and SMMC) rates for each electron-capture reaction, while the black points are the approximate rates given by Eq. 1. Panel (b): The residual differences between \log_{10} of the shell-model rates and the approximate rates for each nucleus in the weak-rate library. An example residual is indicated on panel (a). When the density and temperature of a simulation evolve outside the range of the rate tables (see Table 1), rates are calculated via the approximate routines in order to avoid an artificial cut off imposed by the table boundaries. Rates are estimated between density and temperature grid points via monotonic cubic-spline interpolation as described by Steffen (1990).

liseconds before core bounce. In these final moments, the central density reaches a few times 10^{12} g cm^{-3} , which is large enough that the neutrino mean free path begins to shorten due to coherent scattering on heavy nuclei. This increase in the ν_e -scattering cross section results in a neutrino diffusion time that exceeds the collapse time, thereby trapping the electron neutrinos in the inward flow of matter. After this occurs, the conversion of electrons into electron-neutrinos via electron captures no longer removes leptons from the core. Instead, further electron captures increase the electron-neutrino fraction Y_{ν_e} in order to conserve the now constant lepton fraction and bring the system of electrons and electron neutrinos into equilibrium.

Prior to the work of Langanke et al. (2001a) it was believed that electron captures on free protons were of greater importance than captures on nuclei during collapse. The main considerations involved were that electron capture on free protons has a higher rate owing to a smaller Q -value, and that nuclei with neutron number $N \geq 40$ have full pf -shell single particle states. Thus,

the addition of another neutron via an allowed electron-capture transition would be Fermi-blocked. Langanke et al. (2001a) recognized that the many-body nuclear states have mixed configurations and do not follow a simple Hartree-Fock filling of single particle orbitals. They also suggested that thermal excitation of nucleons to the $g_{9/2}$ orbital creates vacancies in the pf -shell, and together with configuration mixing, electron capture on bound protons is unblocked. Furthermore, because of the low entropy in the core, and the neutron-rich conditions, the abundance of heavy nuclei is several orders of magnitude higher than that of free protons, resulting in a higher overall electron-capture rate. Thus, because electron captures on nuclei dominate, a detailed investigation of the contribution each species has to the deleptonization of the collapsing core, and in particular a determination of which nuclei are most important and therefore deserve further experimental and theoretical focus, would be of great value.

4. CODES & METHODS

4.1. NuLib

In addition to the electron captures rates developed in this paper, other rates are needed to perform core-collapse simulations. The collection of rates we use is contained in NuLib (O’Connor 2015), an open-source, neutrino-interaction library available as a GitHub repository at <http://www.NuLib.org>. NuLib contains routines for calculating electron-type neutrino/antineutrino charged-current absorption opacities on nucleons with corrections for weak magnetism and nucleon recoil based on the formalism of Burrows et al. (2006) and Horowitz (2002). Neutrino emissivities for these processes are determined via Kirchhoff’s law which equates the absorption rate of a equilibrium neutrino distribution to the emission rate of the underlying matter. Elastic scattering of neutrinos on nucleons, and coherent scattering of neutrons on alpha particles and heavy nuclei is also included in NuLib. For the former we include corrections for weak magnetism and nucleon recoil, and for the latter we include corrections from ion-ion correlations (Horowitz 1997), electron polarization, and the nuclear form factor. Inelastic scattering of neutrinos on electrons is included based on the expressions of Bruenn (1985). Emissivities of heavy-lepton neutrino/antineutrino pairs via electron-positron annihilation and nucleon-nucleon Bremsstrahlung are computed ignoring final state neutrino blocking. For neutrino-antineutrino annihilation, instead of computing the non-linear absorption opacity during the simulation, we make use of an effective absorption opacity, which has been shown to be an excellent approximation for core-collapse supernovae (O’Connor 2015).

4.2. GR1D

We test our electron-capture rate implementation, and study the sensitivities of the core-collapse phase to these rates using the code GR1D (O’Connor & Ott 2010; O’Connor 2015). GR1D is an open-source spherically-symmetric general-relativistic neutrino-transport and hydrodynamics code used for studying stellar collapse and the early stages of a core-collapse supernova. For details of the hydrodynamics module of GR1D we refer the reader

to O'Connor & Ott (2010). The neutrino transport is handled through a general-relativistic, energy-dependent two-moment formalism for which extensive details can be found in O'Connor (2015). Our scheme numerically solves for the time evolution of the first two moments of the neutrino distribution function: the neutrino energy density and the neutrino momentum density. The simulations utilize 18 energy groups logarithmically spaced between 0 and 250 MeV. Only electron type neutrinos are evolved until the central density reaches $10^{12} \text{ g cm}^{-3}$, after which electron anti-neutrinos and a characteristic heavy lepton neutrino are included. However, these latter two neutrinos do not become important until core bounce has occurred. Spatial fluxes of the neutrino moments are treated explicitly. Inelastic neutrino-electron scattering is handled explicitly until the central density reaches $10^{12} \text{ g cm}^{-3}$ at which point an implicit treatment is used. Together NuLib and GR1D provide a robust and extendable code base, making them ideal for the present study.

4.3. Neutrino emission via electron capture

Electron capture is associated with the emission of electron neutrinos and so the electron-capture rate is proportional to the integrated spectrum of ν_e emitted per second. The rate for a particular nuclide, as tabulated in the implemented rate tables, is defined as the sum of the rates for each of the individual nuclear transitions

$$\lambda = \sum_{ij} \lambda_{ij}, \quad (3)$$

where indices i and j correspond to levels in the parent and daughter nucleus respectively. The spectra of emitted neutrinos from the electrons capturing on nuclei, described by the matter temperature T and electron chemical potential μ_e , will vary based on the initial and final states involved owing to a different reaction Q-value,

$$Q_{ij}^{\text{EC}} = Q_{g.s.} + E_i - E_j \quad (4)$$

where $Q_{g.s.}$ is the atomic mass difference of the initial and final nuclei, and E_i and E_j are the excitation energies of the populated states in the parent and daughter nucleus respectively. The most comprehensive solution to constructing neutrino spectra would be to coherently sum the spectra of neutrinos emitted from each nuclear transition. However this would rely upon rate tabulations for individual transitions which are not presently available. Thus, we implement an effective neutrino spectra in terms of a single reaction Q-value, q , that is chosen to constrain the average energy of the spectrum to match that from the tabulated rates (Langanke et al. 2001b),

$$n(E_\nu, q) = E_\nu^2 (E_\nu - q)^2 \frac{N}{1 + \exp\{(E_\nu - q - \mu_e)/kT\}} \quad (5)$$

$$\langle E_\nu \rangle = \frac{\int_0^\infty E_\nu n(E_\nu, q) dE_\nu}{\int_0^\infty n(E_\nu, q) dE_\nu} = \frac{\lambda_\nu}{\lambda_{\text{EC}} + \lambda_{\beta^+}}, \quad (6)$$

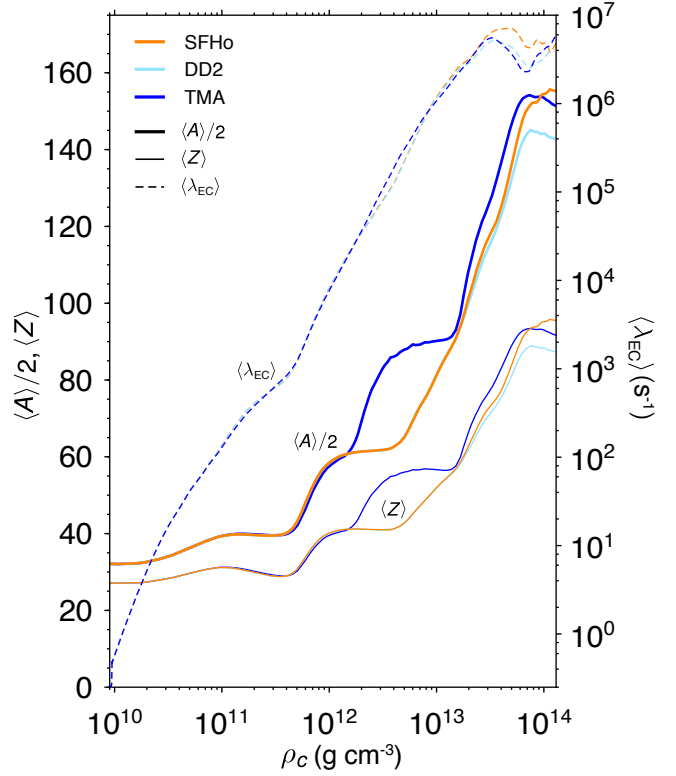


FIG. 3.— The average nuclear mass (divided by two), charge, and electron-capture rate versus central density for the three EOS utilized in this study. The colors indicate different EOS, while the line style indicate which quantity is plotted. All three EOS have nearly identical abundance distributions up to densities of $2 \cdot 10^{12} \text{ g cm}^{-3}$. Beyond this point the TMA EOS has a heavier and slightly more neutron rich mass distribution compared to both SFHo and DD2, but maintains a comparable average electron capture rate overall. These simulations each utilize the s15WW95 progenitor.

where $n(E_\nu, q)$ is the neutrino distribution function and is normalized to the total electron-capture rate for a particular nuclear species. λ_ν , λ_{β^+} , and λ_{EC} are the neutrino energy loss, positron emission, and electron-capture rates respectively. Eq. 6 is solved numerically for the effective Q-value, $q = q_{\text{eff}}$, which then defines the effective neutrino spectrum for the electron-capture reaction of interest at a given ρ , T , and Y_e . The approximate neutrino spectra generated in this way are unable to reproduce complex structure such as double peaking in the true neutrino distribution, which may occur when there is a resonant allowed transition ($Q_{ij}^{\text{EC}} \sim 0$) between an excited parent state and the daughter-nucleus ground state. However, it approximates singly-peaked neutrino distributions quite well (Langanke et al. 2001b). The spectrum is normalized to the total electron-capture rate via Gaussian-Legendre quadrature with an algorithm we developed to adaptively adjust the range of integration to the full width of the spectrum.

Utilizing these spectra, the electron-capture neutrino emissivity for a given nuclear species is calculated as

$$\eta_i(E_k) = \frac{1}{4\pi} E_k n_i n(E_k, q_{\text{eff}}), \quad (7)$$

where the ν_e 's are assumed to be emitted isotropically,

n_i is the number density for the i -th nucleus, $n(E_k, q_{\text{eff}})$ is the neutrino spectra evaluated at the effective Q -value that solves Eq. 6, and E_k indicates the energy of energy group k . Evaluation of the emissivity is done point wise at the centroid of each energy bin, and has units $\text{erg}/(\text{cm}^3 \cdot \text{sr} \cdot \text{s} \cdot \text{MeV})$.

For estimates of the NSE number densities used above, we utilize several EOS from Hempel & Schaffner-Bielich (2010). In particular, we use the SFHo EOS and internally consistent NSE distribution developed by Steiner et al. (2013) for our primary EOS. We also compare with the DD2 (Typel et al. 2010) and TMA (Toki et al. 1995) EOS, each with self-consistent, but different, NSEs. The SFHo and DD2 EOS were chosen because they currently best satisfy both nuclear and astrophysical constraints (Fischer et al. 2014). Instead of meson self-interactions, the DD2 EOS implements density-dependent meson-nucleon couplings which have been used successfully to describe nuclear structure in a wide region of the nuclear chart and have also been tested in heavy-ion collisions (Typel et al. 2010). For nuclear masses, the SFHo and DD2 NSE distributions rely on the Finite Range Drop Model (FRDM) from Möller et al. (1995) and Möller et al. (1997), whereas the TMA EOS utilizes a mass table calculated by Geng et al. (2005). For consistency, in addition to NSE abundances, these mass distributions are also utilized in the calculation of reaction Q -values for use in Eq. 1.

5. SENSITIVITY STUDY

5.1. Reference simulations

In order to establish reference simulations off which variations are performed, we have utilized the widely studied 15 solar mass, solar metallicity progenitor s15WW95 (Woosley & Weaver 1995), as well as s12, s20, and s40 from WH07 (Woosley & Heger 2007), which span the range of stellar compactness $\xi_{2.5}$ (O'Connor & Ott 2011) in this model set. For more details, see the progenitor sensitivity subsection below. For each progenitor we use the SFHo EOS described above, and in addition, for s15WW95 we also employ the DD2 and TMA EOS and NSE distributions.

For each reference simulation, a full complement of neutrino-interaction microphysics is incorporated via NuLib, which includes the newly implemented weak rates library described here. The weak-rate tables were included using the following priority hierarchy: $LMP > LMSH > Oda > Approx.$, ensuring that rates from sources with higher priority are utilized where rate estimates from multiple sources exist. *Approx.* indicates the parameterized rate approximation of Eqs. 1 and 2, which is used for nuclei not included in the tables and for regions of density and temperature which are beyond the limits found in Table 1. For consistency, only tables that derive from shell-model calculations are utilized.

For each progenitor and EOS we perform collapse simulations in GR1D and follow the evolution until at least ~ 100 ms after bounce. The collapse proceeds as described in Section 3. Differences in the collapse evolution for different progenitors stem from the hydrostatic conditions in the cores of these massive stars at the onset of collapse. For stars with large $\xi_{2.5}$, larger central temperatures are needed to balance gravity. This gives lower central densities, and therefore less electron capture during the final

stages of stellar evolution. The range of initial central Y_e goes from ~ 0.422 for the s15WW95 model to ~ 0.447 for the s40WH07 model, or a range of $\sim 6\%$. After neutrino trapping sets in, we see a range of trapped lepton-fraction of $\sim 0.288 - 0.297$, where s40WH07 and s12WH07 have the minimum and maximum trapped Y_l , respectively. The overall higher deleptonization rate for the more compact progenitors is due to both longer collapse times and larger matter temperatures, which enhance the electron-capture rates.

Simulations utilizing different EOS, while holding all else constant, demonstrate only small variations in the density, temperature, and Y_e central-zone trajectories up to bounce. Figure 3 details the abundance distributions for each EOS, as well as the resulting average electron capture rate along a collapse trajectory. The NSE distributions of all three EOS are largely similar early on, but differences in the mass table of the TMA EOS cause it to diverge from the others starting around $1 - 2 \times 10^{12} \text{g cm}^{-3}$. However, differences are seen in the electron-capture rate only after central densities of $2 \times 10^{12} \text{g cm}^{-3}$, where any effect on the evolution is suppressed because of neutrino trapping. Near nuclear saturation density, however, the differences in EOS begin to play a more important role. The density-dependent couplings of the DD2 EOS, for instance, result in higher central temperatures at bounce. However, since the average rate in simulations utilizing each of the EOS are nearly identical, they result in a difference of trapped lepton-fraction of only a fraction of a percent. For more information on the sensitivity of the electron and lepton fractions to the EOS during collapse see Fischer et al. (2014).

Together, these reference calculations span a wide range of progenitor and EOS dependences that ensure a configuration-independent assessment of the core-collapse sensitivity to electron capture on nuclei, and furthermore demonstrate the universality of collapse. In what follows, we detail the results primarily for variations on the s15WW95+SFHo reference simulation, but describe any significant differences, where they exist, in relation to variations on the other progenitor+EOS reference simulations.

5.2. Species dependent sensitivity

To understand the sensitivity of core-collapse to different regions of electron capturing nuclei, we use the central zone collapse profile from our reference simulation to decompose the change of the electron fraction with time, \dot{Y}_e , into the electron captures of each nuclear species. While using only the central zone is an approximation, we justify this by noting the observation by Liebendorfer (2005) that the electron fraction profiles typically correlate quite well with density during the collapse phase. Therefore, matter will generally have the same electron capture history. We calculate \dot{Y}_e and account for ν_e re-absorption in the following energy-dependent way,

$$\dot{Y}_e^i = \frac{4\pi\alpha}{\rho N_a} \sum_k \frac{\Delta\epsilon_k \cdot \eta_i(\epsilon_k)}{\epsilon_k} \cdot \left(1 - \frac{E_k}{B_k}\right) \quad (8)$$

where \dot{Y}_e^i is the time derivative of the electron fraction due to electron captures on the i th nuclear species, α accounts for the general relativistic time dilation, N_a is Avogadro's

constant, ρ is the density, ϵ_k is the energy of the k th energy bin, $\Delta\epsilon_k$ is the k th energy bin width, η_i is the emissivity of species i and $1 - \frac{E_k}{B_k}$ is the neutrino blocking factor that accounts for re-absorption as collapse approaches weak equilibrium. Along with a hydrodynamical correction due to advection of electrons into the central zone, the time integral of Eq. 8 added for all nuclei reproduces the full time dependent Y_e profile of the central zone during collapse, indicating that electron captures on heavy nuclei singularly drive the deleptonization of the central zone.

With this method, the deleptonization history due to each nucleus can be individually investigated. At these densities and temperatures, NSE diversifies the abundant nuclei, ensuring that no single nucleus dominates the deleptonization. There are, however, subsets of nuclei that contribute more than others to the reduction of Y_e . A nuclear-mass dependence can be studied by binning the the contribution to $|\dot{Y}_e|$ from each nuclide into nuclear mass bins and tracking the evolution of each region up to neutrino trapping. Figure 4a plots the deleptonization rate in the core for different nuclear mass bins, as the central Y_e progresses from its progenitor value to its value when weak equilibrium is achieved, just prior to bounce. Early on, before the collapse becomes strongly dynamical, nuclei in both the mass range $25 < A < 65$ (*sd+pf*-shell) and those in the $65 < A < 105$ (*pf*/*sdg*-shell) comprise the main component of the deleptonization. However, during the strongest push toward neutron-rich conditions, where Y_e rapidly changes from ~ 0.41 to ~ 0.28 , nuclei with mass $A > 65$ dominate the evolution as seen by the red and light blue curves in Figure 4a. Unfortunately, the most precise electron-capture rate estimates fall below this region and instead, the rates are set primarily by the approximation of Eq. 1.

It is also useful to understand the specific nuclei that have the largest integrated contribution to core deleptonization up to neutrino trapping. In panel (b) of Figure 4 we plot the 500 nuclei with the largest integrated $|\dot{Y}_e|$ from $t = 0$ to the trapping time—when densities are in excess of $2 \cdot 10^{12} \text{ g cm}^{-3}$. This reveals the channel through which the bulk of electron captures operate. The central electron-fraction at the trapping density is reproduced by subtracting the sum of this quantity over all nuclear species from the initial electron-fraction,

$$Y_e(t = t_{\text{trapping}}) \simeq Y_e(t = 0) - \sum_i \Delta Y_e^i, \quad (9)$$

where ΔY_e^i is shown in Figure 4b, and the component of Y_e due to advection of electrons into the central zone (otherwise making this relation exact) is left out for simplicity. Within the *pf*/*g* and *sd*/*g*-shells we find that primary contributors to the deleptonization phase of collapse are neutron rich nuclei near the $N=50$ and $N=82$ closed neutron shells.

To confirm these results, we also gauge the sensitivity of the collapse phase to localized groups of nuclei by employing a statistical resampling technique where sets of nuclei are removed from the simulation. This method is based on well known statistical resampling methods such as bootstrap and jackknife resampling (Wu 1986). Specifically, a rectangular region centered on a nucleus and spanning all nuclei within ± 3 isobars and

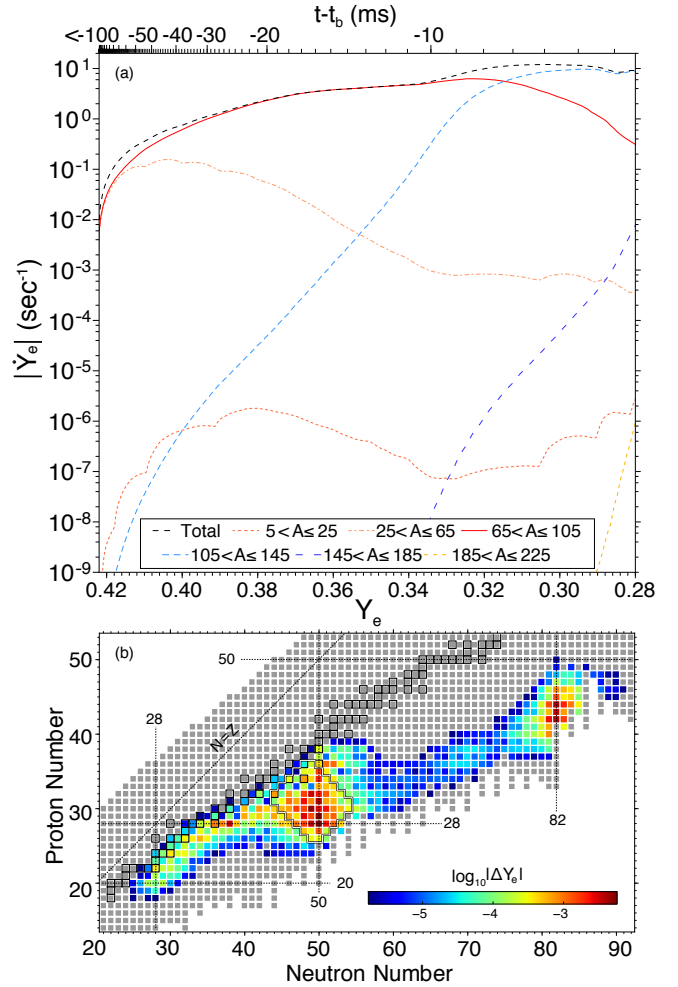


FIG. 4.— (a) The contribution of nuclear electron capture to the change of the matter electron-fraction with time. The contours are the binned sums of $|\dot{Y}_e|$ for each species in several mass regions. For reference, the central density at $t - t_b = -20, -10, -5, -2,$ and -1 ms is $1.41 \cdot 10^{11}, 4.06 \cdot 10^{11}, 1.42 \cdot 10^{12}, 8.49 \cdot 10^{12}, 3.30 \cdot 10^{13} \text{ g cm}^{-3}$ respectively. (b) Top 500 electron capturing nuclei with the largest absolute change to the electron fraction up to neutrino trapping. The color scale indicates $|\dot{Y}_e|$ integrated up to the trapping time, occurring when $\rho_c \sim 2 \cdot 10^{12} \text{ g cm}^{-3}$, such that the total electron-fraction at this point is equal to its initial value less the sum of ΔY_e , the plotted quantity, over all nuclides. Calculations are based on the s15WW95+SFHo reference simulation. The rectangular outline indicates the size of the sampling region used in the statistical resampling study, and also the set of nuclei which exhibited the largest changes to the simulations when excluded from the electron-capture calculations.

± 5 isobaric chains is removed from the calculation of the electron-capture neutrino emissivity. An example of such a removed region is drawn on Figure 4b. This technique is employed in 48 simulations with resampling performed uniformly across the nuclear chart. Using this technique we find the simulations are most sensitive to nuclei in the mass range 74-84 with $Z/A (= Y_e)$ between 0.36-0.44, corresponding to nuclei near ^{78}Ni , ^{79}Cu , and ^{79}Zn . These results agree with the \dot{Y}_e calculations performed above, and indicate that species near the $N=50$ magic number have the largest contribution in magnitude to the change in the electron fraction overall. The impact of removing these species from the simulation corresponded to a change of inner-core mass at bounce of $\gtrsim 10\%$, whereas

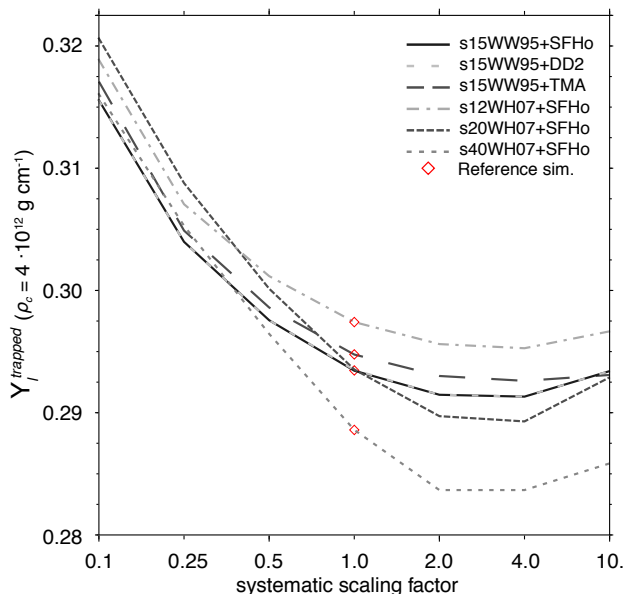


FIG. 5.— Projection of the (trapped) lepton fraction at $\rho_c = 4 \cdot 10^{12} \text{ g cm}^{-3}$ as a function of the electron-capture rate scaling factor for progenitor+EOS reference simulation. In all the cases the lepton fraction begins to increase if the capture rate becomes too high because of a dramatic increase in the electron neutrino absorption cross section. The asymmetry seen here indicates that those quantities which depend on $Y_{l/e}$ are likely to be more sensitive to a reduction of the electron-capture rates due to a systematic overestimate in the base rates, than they are to an increase due to an underestimate.

resampling in other regions resulted in variations of only a few percent.

The electron-capture rates for these nuclides rely entirely on the approximation of Eqs. 1 and 2, which were fit originally to rates of lower-mass mid-shell nuclei near stability. Therefore, in the region indicated by the above two studies, the approximation is largely uncertain and may be systematically off by a significant amount. For instance, these estimates do not account for nuclear structure effects that may occur near the $N=50$ closed neutron shell. Depending on the nuclear configurations, thermal excitations, and increasing dependence on forbidden transitions, Pauli blocking may considerably reduce the electron-capture rates in this area. Given that the change of inner-core mass at bounce was largest when the rates of these nuclides were decreased to zero as compared to any other set, and that without any evaluative measurements the uncertainties in these rates remain large, experimental and theoretical work should focus here. Any substantial changes to the electron-capture rate estimates for these nuclei will likely have a relatively large impact on simulation predictions for the PNS formation, and will therefore help to constrain important collapse and pre-explosion phase quantities.

5.3. Systematic variations

To study the strongest impact of variations in the electron-capture rates, we perform simulations in which the rate for each $A > 4$ nuclide is systematically scaled by factors of 10, 4, 2, 0.5, 0.25, and 0.1. In this way, the structure of the rates as seen in Figure 2 is preserved (the lower panel of residuals is unaffected), but the dis-

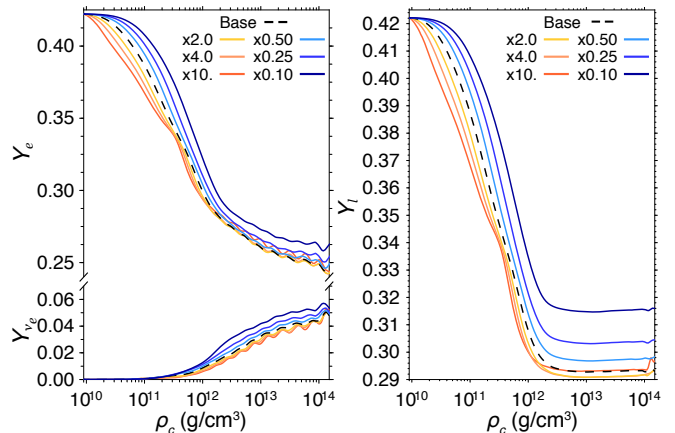


FIG. 6.— Comparison of the central electron, electron-neutrino (left) and lepton (right) fractions in which the nuclear electron-capture rate for every species has been scaled by factors shown in the legend. Warmer colors indicate a higher overall electron capture rate, and cooler colors indicate a lower rate. The dashed black line indicates the reference s15WW95+SFHo simulation.

tribution of rates is shifted to larger or smaller values depending on the scaling factor. Systematic shifts of the rates emphasize the role of electron capture as a regulator for entropy and temperature in the simulations. By increasing the rates, more neutrinos are emitted and escape during the initial stages of collapse, thereby increasing the evaporative neutrino-cooling. Furthermore, because the dominant source of matter pressure is electron degeneracy, increased electron-capture rates accelerate the collapse. This impacts the matter profiles outside the shock in the early post-bounce phase. Decreasing the rates has the opposite effect, the entropy, temperature, and electron fraction of the core are significantly higher because less cooling takes place.

The evolution prior to and right at $\rho_c = 2 \cdot 10^{12} \text{ g cm}^{-3}$ (which is the density that defines neutrino trapping) is what sets the final value of the trapped lepton and electron fractions, which are important due to their direct impact on the formation of the PNS. For all the reference simulations we observe a minimum in the trapped lepton fraction occurring for a systematic scaling factor of approximately four. The minimum that forms can be seen in Figure 5. Scaling by ten slightly reverses the downward trend, and increases the trapped lepton-fraction from its minimum value. This behavior is the result of electron-neutrino capture on heavy nuclei becoming the primary source of opacity, exceeding what is typical as a result of coherent ν_e -scattering. When the rates have been enhanced by a factor of ten, the ratio of the absorption and scattering opacities, κ_a/κ_s , surpasses unity already by central densities of $3 \cdot 10^{11} \text{ g cm}^{-3}$ and $\kappa_a \sim 4\kappa_s$ by the time $\rho_c = 10^{12} \text{ g cm}^{-3}$. Absorption cross sections are then large enough to trigger an early onset of neutrino trapping at densities lower than what is found for the reference rates. The consequence is that electron capture has a smaller window of deleptonization, leading ultimately to a higher Y_l overall.

The range of electron fractions near core bounce is commensurate with the range of trapped lepton-fractions so far described, see Figure 6. As mentioned above, variations of Y_e (and Y_l) on this level are of importance due to its direct impact on the formation of the PNS and the su-

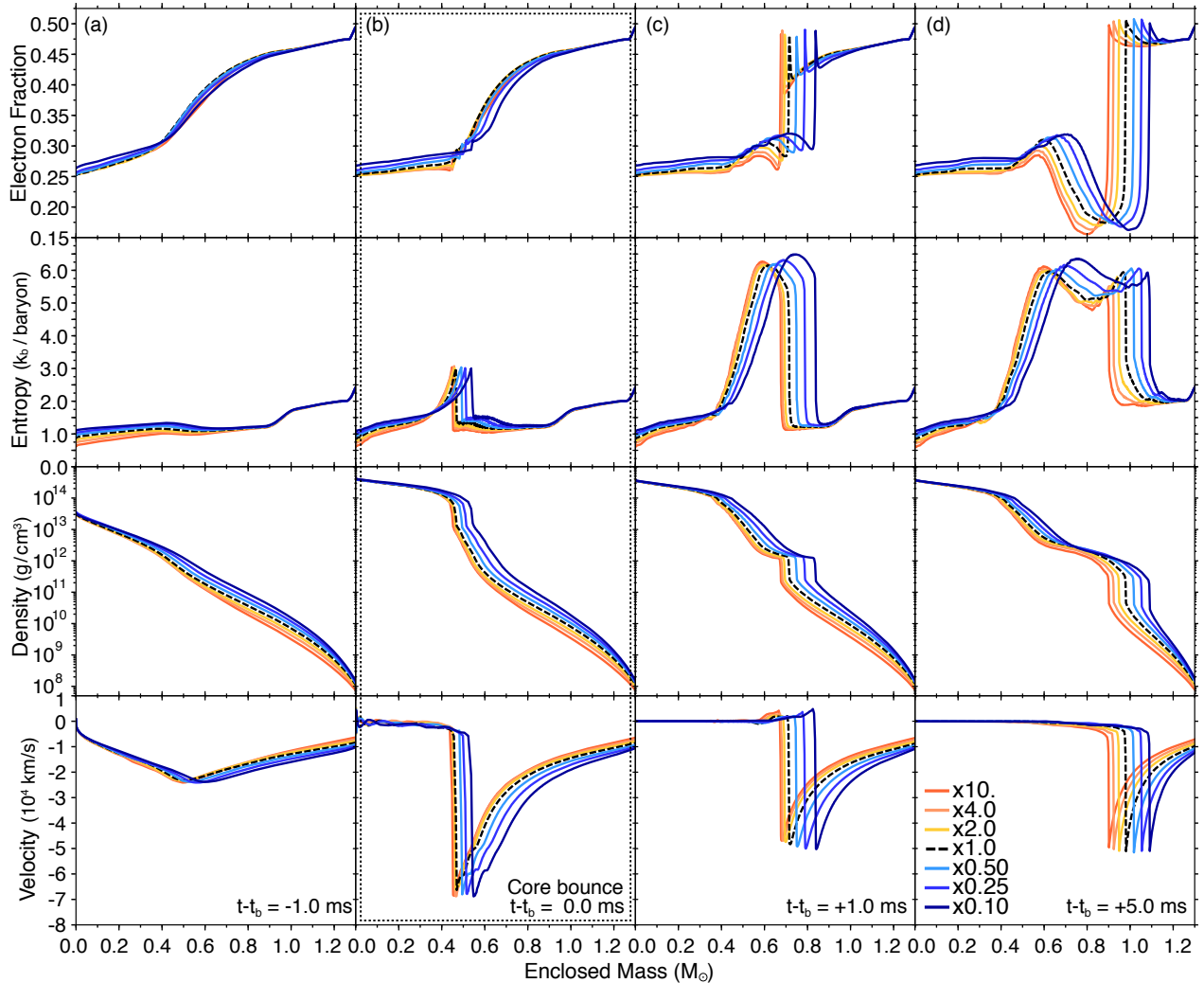


FIG. 7.— The electron fraction, entropy, density, and velocity as a function of enclosed mass at four times during a core-collapse simulation, spanning 6 ms around bounce, including the collapse phase just after the onset of neutrino trapping (a), core bounce (b), and 1 ms (c) and 5 ms (d) after bounce during which the shock has begun its outward trajectory. The reference simulation (s15WW95+SFHo) is shown in dashed black. Simulations shown in color have electron-capture rates scaled systematically for all species by factors of 10, 4, 2, 0.5, 0.25, and 0.1. Core bounce ($t - t_b = 0$) shown in panel (b) is defined as when the entropy at the shock front exceeds $3.0 k_b/\text{baryon}$.

pernova shock. Electron fraction, entropy, density and velocity profiles are shown in Figure 7 for s15WW95+SFHo at $-1, 0, 1,$ and 5 milliseconds relative to bounce. Of particular interest, we find that the mass of the forming PNS inner-core at bounce, seen as the mass behind the steep velocity gradient in panel (b), varies on the order of $\sim 0.1 M_\odot$, and up to $\sim 0.2 M_\odot$ five milliseconds after bounce. The asymmetry observed in the trapped-lepton fraction, where scaling the rates by 0.1 had a more dramatic effect than scaling by 10, translates directly to the variation of the inner-core mass at bounce ($+16/-4\%$ from the reference). The result we find is that the forming PNS has a lower bound on the inner-core mass at bounce over the range of electron-capture rates explored. Because the rates are already high, and therefore the absorption opacity is already almost comparable to the scattering opacity, the range of inner-core mass at bounce comes mainly from simulations with decreased rates relative to the base simulation.

In addition to the direct impact on core dynamics and

structure, the neutrino emission at bounce is found to be very sensitive to these variations. Figure 8 shows the neutrino luminosity 500 km from the center for the different neutrino species as a function of time. Prior to bounce the ν_e -luminosity begins to rise from electron captures on bound protons in nuclei, but is quickly regulated by neutrino trapping, causing a down turn in the luminosity. During this time the core is very sensitive to the nuclear electron-capture rates as the entropy is low enough that heavy nuclei dominate the available mass. Scaling the rates for each nucleus using the same systematic factors results in a 40% variation of the ν_e -luminosity before bounce. During bounce, the electron-neutrino burst—seen as the peak luminosity in the left panel of Figure 8—is powered primarily by electron capture on free protons. The core-bounce and shock liberates nucleons from their bound states and the entropy rises causing a significant increase in the nucleon and light particle abundances. That said, while the electron-capture rate on free protons, λ_p^{EC} , is not adjusted in these simulations, a range

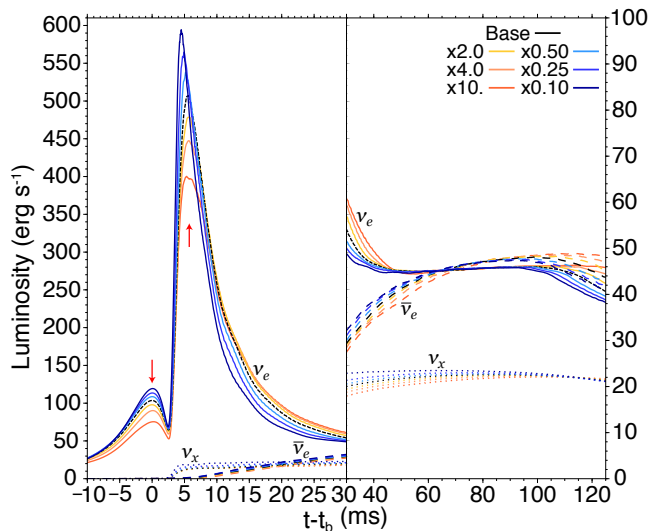


FIG. 8.— The neutrino luminosity as measured at a radius of 500 km as a function of time after bounce in our s15WW95+SFHo simulation set. Electron-capture rate scaling factors are shown in the legend, where contours with warmer colors have higher rates, and cooler colors have lower rates. While the peak electron-neutrino luminosity is considered particularly stable across core-collapse simulations, it varies significantly with variations of the electron-capture rates on medium-heavy nuclei. When the rates are at their lowest ($\times 0.1$ case), the shock reaches the neutrinosphere more quickly than in the other simulations. This results in a larger luminosity in the peak electron-neutrino burst because more ν_e s are able to stream out of the core at early times. The opposite is true when the rates are higher, the neutrinosphere and shock converge much more slowly, and so the neutrinos spend more time diffusing out of the inner core, reducing the peak luminosity but distributing it out to later times.

of $\pm 20\%$ relative to the reference peak ν_e -luminosity is observed.

We find that these dramatic variations of the peak electron neutrino luminosity are a result of alterations to the neutrinosphere and shock convergence-timescale. Specifically, when electron captures on nuclei are weaker (scaling by 0.1), the inner-core mass that forms at bounce is significantly larger. This results in more kinetic energy transferred to the shock, allowing it to sweep up mass more quickly. In Figure 7 this can be seen by the broadening of the distribution of shock locations in mass between the different simulations in the velocity plot 5 ms after bounce (bottom-right) as compared to $t - t_b = 0$. Also, with a weaker overall rate the opacity will be lower, allowing the neutrinosphere to move in to lower radii more quickly. The combination of these effects result in the shock and neutrinosphere radii converging earlier for the simulations with lower electron-capture rates, and later for simulations with higher rates, up to a difference on the order of 3.5 ms. Thus, electron capture on protons liberated by the shock produce neutrinos that are able to reach the neutrinosphere earlier and freely stream away, contributing to a larger ν_e peak luminosity when the nuclear electron capture rate is systematically lower. On the other hand, when the nuclear electron capture rate is high, the emitted neutrinos diffuse more slowly through the core, and reach the neutrinosphere at later times, thus strongly quenching the peak luminosity but spreading out the emission to later times. Due to the high luminosity of the electron-neutrino burst near the time of bounce, it

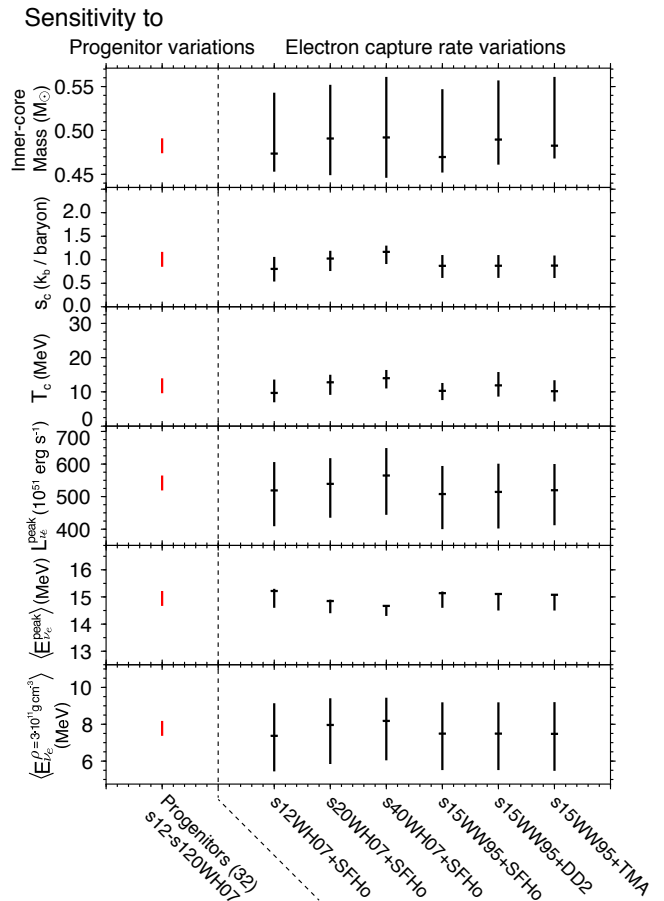


FIG. 9.— The full range of sensitivity of the PNS inner-core mass, central entropy, and central temperature at bounce as well as the peak ν_e -luminosity, the peak average ν_e energy, and the average ν_e energy prior to neutrino trapping, owing to variations of the progenitor model and electron-capture rates. Thirty two progenitors were utilized from the WH07 model set of Woosley & Heger (2007) for producing the progenitor bars (red) in the figure. Each bar of the electron-capture rate variations derives from simulations where the rates have been systematically scaled by factors of 10, 4, 2, 0.5, 0.25, and 0.1. The horizontal tick represents the value of the reference simulation for the tested Progenitor + EOS combination. The window ranges are chosen so that the progenitor sensitivity bars are of equal size across each of the plotted parameters.

is a candidate for detection from a galactic core-collapse supernovae in Earth-based detectors sensitive to electron neutrinos, e.g. those with a detector volume composed of liquid Argon. And while such measurements are not presently of high enough precision to resolve each variation seen here, they may indicate the total amount of electron capture occurring at core bounce.

5.3.1. Progenitor model sensitivity

In order to evaluate the significance of the electron-capture systematic sensitivity studies described so far, we have chosen to test against a study of the progenitor dependence of the core-collapse phase. Drawing from the larger set of progenitors from which the reference progenitors of the electron-capture study belong, the 2007 non-rotating solar-metallicity single-star model set from the stellar evolution code KEPLER (Woosley & Heger 2007) was utilized. This model set contains the presupernova configuration of 32 stars ranging in zero-age-main-sequence (ZAMS) mass from $12 M_\odot$ to $120 M_\odot$ —s12WH07 and

s120WH07 respectively. Simulations of these progenitors exhibit a $\sim 3.5\%$ range of trapped lepton-fraction (0.288 – 0.298), a $\sim 4\%$ range of inner-core mass at bounce (0.473 – 0.491 M_\odot), and a $\sim 9\%$ range of electron-neutrino peak luminosity ($5.19 - 5.65 \cdot 10^{53}$ erg s $^{-1}$) during the neutrino flash occurring just after core bounce.

Figure 9 compares the progenitor model and electron-capture rate dependence of several structural and neutrino quantities during collapse. The range of inner-core mass and peak ν_e luminosity seen from employing the WH07 progenitor model set are each approximately a factor of 5 smaller than the ranges seen from varying the electron-capture rates across all progenitor+EOS references. On the other hand, the range of central entropies and temperatures at bounce are comparable between the two sensitivity studies. The ν_e average energies just prior to neutrino trapping and during the deleptonization burst are also compared in Fig. 9. The neutrinos emitted during the luminous burst just following core bounce are of higher energy than those emitted earlier because they arise primarily from electron capture on free protons. They also decouple from the core at a much hotter and denser neutrinosphere than prior to bounce, yielding higher energy neutrinos. In both of the sensitivity studies, variations of the electron-capture rates and of the initial stellar models, we find that the range of average neutrino energy during peak emission is comparable ($\approx \pm 0.5$ MeV).

While captures on free protons contribute only marginally to deleptonization in the central zone, further out in the iron core, where the densities are lower (and Y_e 's are higher), electron captures on protons contribute to the deleptonization, especially in cases where we suppress electron captures on nuclei. The capture of electrons on these free protons produces neutrinos of a higher average energy, commensurate with the large spread seen in the bottom panel of Fig. 9 (which is taken when the central density is 3×10^{11} g cm $^{-3}$, but present from the onset of collapse). Another contribution to the energy spread is the systematic shift of electron captures to more neutron rich nuclei as the electron-capture rates are increased and the matter becomes more neutron rich. These neutron-rich nuclei have more negative Q-values, yielding lower energy neutrino emission. Both of these effects result in a dispersion of average neutrino energies early on that is several factors larger than what is seen in the progenitor simulations.

Finally, we note that while the peak luminosity is only weakly dependent on the progenitor model, the post-bounce pre-explosion luminosity of all six neutrino species have strong progenitor dependences (O'Connor & Ott 2013), and we find these pre-explosion luminosities are much less sensitive to the nuclear electron-capture rates comparatively—see panel (b) of Figure 8. The diverging of the luminosities seen at $t - t_b = 120$ ms is due only to the difference in collapse times between the simulations which carries over to the evolution of the mass accretion rate after bounce.

5.4. Monte-Carlo variations

In addition to the possibility of systematic errors in the electron-capture rates, we also explore the effect of statistically distributed variations. Such an investigation is of great importance if the effect of an approximation such as

Eq. 1 is to be understood. The main flaw in a continuous function for rate estimation across many nuclear species is the loss of structure, which would otherwise serve to statistically distribute the rates on a reaction by reaction basis (see Fig 2). To study this effect we performed a Monte-Carlo (MC) variation of the electron-capture rates. Using an analytic description of the electron-capture rate distributions, such as a Gaussian or Poisson distribution, is likely to be inaccurate. Instead, we MC adjust the approximate rate for each species by adding to its $\log_{10}(\lambda_{\text{EC}})$ a value randomly chosen from a distribution created from the residuals of the tabulated rates and the approximate rates, i.e.

$$\log_{10}(\lambda_{\text{EC}}^{i,\text{table}}) - \log_{10}(\lambda_{\text{EC}}^{i,\text{Eq.1}}) \quad (10)$$

where i is an index running over all the tabulated reactions.

In constructing this distribution, it is important also to preserve the Q-value dependence of the residuals that can be seen in Figure 2b. We do this by separating the residual distribution into subsets so that the reaction-rate residuals in each subset have similar Q-values. To do so we have chosen a Q-value binning of 2.5 MeV, but have also tested binnings of 5.0 MeV and 10.0 MeV which resolve the Q-dependence less, but have more counts per bin from which to sample. With this method we MC generate pseudo electron-capture rates that retain the Q-value dependence of Eq. 1, but statistically distribute the approximate rate according to the variance of the rates calculated in the shell-model. Seven simulations for each binning were performed.

As mentioned before, at low densities the electron-capture rate depends strongly on the energy levels of the initial and final nuclides because the electron chemical potential is comparable to the excitation energies of the allowed Gamow-Teller transitions. As the electron chemical potential increases, it encompasses a larger range of excitation energies which results in the electron-capture rate becoming sensitive primarily to the total strength. In the low-density case of Figure 2a the approximation of Eq. 1 while appearing to decently reproduce the mean of the shell-model rates, actually has a mean approximately a factor of two lower than the tabulated rates. As the density increases, this difference between the mean electron-capture rate estimated by the approximation and the shell-model rates decrease. Thus, the approximation better reproduces the mean rate in the high density case of Figure 2a. Because our MC simulations are based on residual distributions of the tabulated rates and the approximation, the average rate produced in each MC trial also has this bias.

In Figure 10 we plot the min-to-max band representing the range of lepton fraction observed from all of the MC simulations. The band drawn corresponds to a 2.5 MeV binning of the residual distributions from which the MC sampling was performed. For the reasons just described, the band has lower electron and lepton fractions than the reference at low densities, but becomes more statistically distributed around the reference at higher densities, near $5 \cdot 10^{11}$ g cm $^{-3}$. The lepton fraction band width varies from about a half percent initially, to its largest value of $\sim 2.5\%$ just before neutrino trapping, and then decreases back to $\sim 1.5\%$ before bounce. Altogether, we observe no

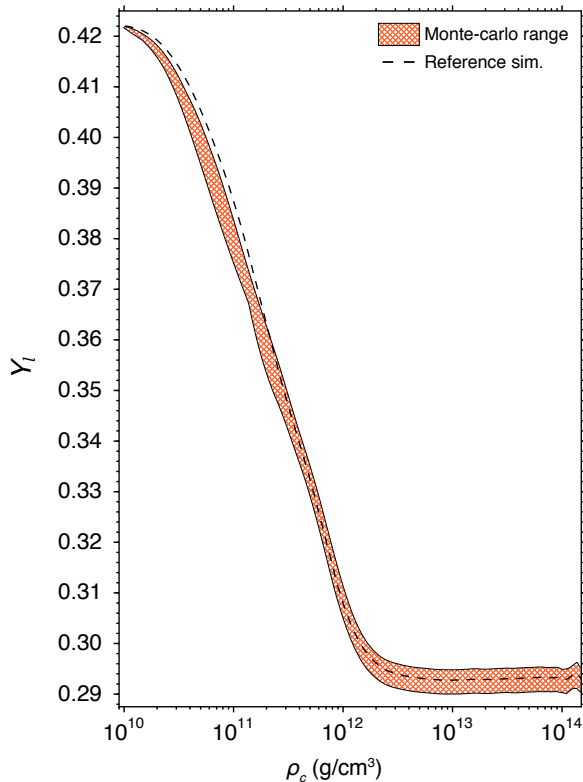


FIG. 10.— Lepton fraction band as a function of central density for the Monte Carlo (MC) described in the text. The band represents data points from seven MC simulations based on the s15WW95+SFHo reference, where the band width represents the min to max range of Y_l . The rates are varied by drawing from the Q-value dependent residual function shown in Figure 2 after binning it into 2.5 MeV energy bins. This binning was chosen as it best tracks the Q-value dependence of the residual distribution.

significant impact on the core dynamics or the neutrino transport and therefore conclude that any statistically distributed scatter in the estimations of the electron-capture rates, such as those seen in Figure 2, will likely not impact the models.

6. CONCLUSION

Nuclear electron capture has long been understood to play an important role in the dynamics of core-collapse supernovae and large efforts have been undertaken to produce reliable estimates of electron-capture rates for astrophysical contexts. Although significant progress has been made in benchmarking theoretical electron-capture rates by comparison with charge-exchange experiments (especially using shell-model calculations) (Cole et al. 2012), large uncertainties remain for neutron-rich nuclei and nuclei beyond $A=65$. Furthermore, sophisticated shell-model estimates for electron-capture rates exist only for a small subset of the large number of nuclei that contribute strongly. In this work we explore the implications of uncertainties in the electron-capture rate estimates for the core-collapse and early post-bounce phases of fully self consistent, general relativistic, core-collapse supernova simulations with comprehensive neutrino transport.

6.1. Most important nuclei

For the reference simulation we calculate the contribution of each nucleus to core deleptonization and also

perform a statistical resampling study, both of which identify those species whose rate should be known most precisely due to their significance in the simulations. With the given set of electron capture rates—from shell-model estimates to the approximate estimates of Eqs. 1 and 2—we find that the simulations are most sensitive to neutron rich nuclei in the upper pf and pfg/sdg -shells.

Specifically, in these simulations nuclei near the $A\sim 80$, $N\sim 50$ closed neutron shell contribute the bulk of core deleptonization, and when removed from the simulations result in noticeable changes to the protoneutron star formation, with a significantly larger impact than when any other group of nuclei are removed. However, because sophisticated estimates from nuclear theory are not available for individual nuclei in this region, the electron-capture rates for these species have been accounted for in the past via simple averaging techniques and in this work via an approximation that has been fit to the LMP rate set. While this approximation reasonably reproduces the average electron capture rate for sd and pf shell nuclei near stability, rates for heavier neutron-rich nuclides will likely diverge from what is predicted by this parameterization.

6.2. Impact of uncertainties

We evaluate the impact such uncertainties may have by varying the electron-capture rates for more than 6000 nuclei statistically, about the approximate prediction, and also systematically. On one hand, we find that statistical variations of electron-capture rates effect the overall dynamics and neutrino emission only weakly, producing marginal changes to the simulations. These findings indicate that the lack of structural variation that distributes the rate estimates from one species to the next is not crucial to the simulations.

On the other hand, the average electron capture rate across a region of nuclei strongly determines the overall impact of those constituent nuclei. By systematically varying the electron-capture rates by factors between 10 and 0.1 we observe dramatic variations in the inner-core mass (+16/-4%) and the electron-neutrino luminosity ($\pm 20\%$) at and near bounce, respectively. Comparing with 32 simulations utilizing different progenitor models, we find that this range of inner-core mass and peak neutrino-luminosity is 5 times as large as that seen when varying the progenitor models.

We also find that the nuclear electron-capture rates are already large enough in the reference simulations that increasing them beyond their base values has a considerably smaller effect than decreasing them. This has compelling implications. Rates for $A\sim 80$ nuclei near the $N=50$ shell gap, which have been shown in this work to be the primary contributors to the overall impact of electron captures during core collapse, may be overestimated by Eq. 1 due to Fermi-blocking at the closed neutron shell. Combined with a greater overall sensitivity to the systematic decrease in electron-capture rates, changes to the collapse and early post-bounce phases of the simulations may be as significant as those seen in this study if the current rates of these nuclei are found to be overestimated.

6.3. Goals for future studies

For these reasons, it is important that experimental and theoretical efforts be aimed at nuclei which span

the region on the chart of isotopes between stability and the neutron drip-line in both the *pf* and *pfg/sdg* model spaces, and further expand on the work that has been carried out for (near-)stable nuclei in the *pf*-shell. Since data from (n,p)-type charge-exchange experiments for nuclei in the *pfg/sdg*-shell and for neutron-rich nuclei in the *pf* and *pfg/sdg*-shell are scarce, new experiments are required to obtain a sufficient set of data to benchmark current and future theoretical estimates. To this end, presently feasible experiments on neutron-rich nuclei at and near stability with $60 < A < 120$ should add to the few cases that have been measured in this region. With the higher beam intensities that will be available at next generation rare isotope facilities, future experimental programs should focus on the neutron-rich component of the primary electron-capture channel shown in Figure 4b. In particular, investigation of nuclei in the $A \sim 80$ and $N \sim 50$ region should take precedence, as changes to their electron-capture rates will significantly constrain the core-collapse dependence on nuclear electron-capture.

7. ACKNOWLEDGEMENTS

The authors would like to thank Gabriel Martínez-Pinedo and Raph Hix for valuable discussions, as well as the underlying rate tables from which much of this work was based. We would also like to thank Christian Ott for his support. CS would like to thank CITA for their hospitality and support while carrying out a portion of this research. This material is based upon work supported by the National Science Foundation under Grants No. PHY-1430152 (JINA Center for the Evolution of the Elements) and No. PHY-1102511, by the Department of Energy (DOE) National Nuclear Security Administration under award number DE-NA0000979, and by NASA through Hubble Fellowship grant 51344.001-A awarded by the Space Telescope Science Institute, which is operated by the Association of Universities for Research in Astronomy, Inc., for NASA, under contract NAS5-26555. Some computations were performed on the Zwicky cluster at Caltech, which is supported by the Sherman Fairchild Foundation and by NSF award PHY-0960291.

REFERENCES

- Bethe, H., Brown, G., Applegate, J., & Lattimer, J. 1979, Nuclear Physics A, 324, 487
- Brachwitz, F., Dean, D. J., Hix, W. R., et al. 2000, The Astrophysical Journal, 536, 934
- Bruenn, S. W. 1985, The Astrophysical Journal Supplement Series, 58, 771
- Burrows, A., Reddy, S., & Thompson, T. a. 2006, Nuclear Physics A, 777, 356
- Cole, a. L., Anderson, T. S., Zegers, R. G. T., et al. 2012, Physical Review C, 86, 015809
- Dzhioev, A. A., Vdovin, A. I., Ponomarev, V. Y., et al. 2010, Phys. Rev. C, 81, 015804
- Fischer, T., Hempel, M., Sagert, I., Suwa, Y., & Schaffner-Bielich, J. 2014, The European Physical Journal A, 50, 46
- Fuller, G. M., Fowler, W. A., & Newman, M. J. 1982, The Astrophysical Journal, 252, 715
- . 1985, The Astrophysical Journal, 293, 1
- Geng, L., Toki, H., & Meng, J. 2005, Progress of Theoretical Physics, 113, 785
- Goriely, S., Bauswein, A., Just, O., Pllumbi, E., & Janka, H.-T. 2015, Monthly Notices of the Royal Astronomical Society, 452, 3894
- Gupta, S., Brown, E. F., Schatz, H., Möller, P., & Kratz, K.-L. 2007, The Astrophysical Journal, 662, 1188
- Heger, A., Langanke, K., Martínez-Pinedo, G., & Woosley, S. E. 2001, Phys. Rev. Lett., 86, 1678
- Hempel, M., & Schaffner-Bielich, J. 2010, Nuclear Physics A, 837, 210
- Hix, W. R., Messer, O. E. B., Mezzacappa, A., et al. 2003, Physical Review Letters, 91, 201102
- Honma, M., Otsuka, T., Brown, B., & Mizusaki, T. 2005, The European Physical Journal A - Hadrons and Nuclei, 25, 499
- Horowitz, C. J. 1997, Physical Review D, 55, 4577
- . 2002, Physical Review D, 65, 043001
- Iliadis, C. 2007, Nuclear Physics of Stars (Wiley-VCH Verlag)
- Iwamoto, K., Brachwitz, F., Nomoto, K., et al. 1999, The Astrophysical Journal Supplement Series, 125, 439
- Janka, H.-T., Langanke, K., Marek, A., Martínez-Pinedo, G., & Müller, B. 2007, Physics Reports, 442, 38, the Hans Bethe Centennial Volume 1906-2006
- Juodagalvis, A., Langanke, K., Hix, W., Martínez-Pinedo, G., & Sampaio, J. 2010, Nuclear Physics A, 848, 454
- Juodagalvis, A., Sampaio, J. M., Langanke, K., & Hix, W. R. 2008, Journal of Physics G: Nuclear and Particle Physics, 35, 014031
- Langanke, K., Kolbe, E., & Dean, D. J. 2001a, Physical Review C, 63, 032801
- Langanke, K., & Martínez-Pinedo, G. 2000, Nuclear Physics A, 673, 481
- . 2003, Reviews of Modern Physics, 75, 819
- Langanke, K., Martínez-Pinedo, G., & Sampaio, J. 2001b, Physical Review C, 64, 055801
- Langanke, K., & Martínez-Pinedo, G. 2014, Nuclear Physics A, 928, 305, special Issue Dedicated to the Memory of Gerald E Brown (1926-2013)
- Langanke, K., Martínez-Pinedo, G., Sampaio, J. M., et al. 2003, Phys. Rev. Lett., 90, 241102
- Liebendorfer, M. 2005, The Astrophysical Journal, 633, 1042
- Martínez-Pinedo, G., Lam, Y. H., Langanke, K., Zegers, R. G. T., & Sullivan, C. 2014, Physical Review C, 89, 045806
- Martínez-Pinedo, G., Langanke, K., & Dean, D. J. 2000, The Astrophysical Journal Supplement Series, 126, 493
- Möller, P., Nix, J., & Kratz, K.-L. 1997, Atomic Data and Nuclear Data Tables, 66, 131
- Möller, P., Nix, J., Myers, W., & Swiatecki, W. 1995, Atomic Data and Nuclear Data Tables, 59, 185
- Möller, P., & Randrup, J. 1990, Nuclear Physics A, 514, 1
- Nabi, J.-U., & Klapdor-Kleingrothaus, H. V. 2004, Atomic Data and Nuclear Data Tables, 88, 237
- Niu, Y. F., Paar, N., Vretenar, D., & Meng, J. 2011, Phys. Rev. C, 83, 045807
- Noji, S., Zegers, R., Austin, S. M., et al. 2014, Physical Review Letters, 112, 252501
- O'Connor, E. 2015, The Astrophysical Journal Supplement Series, 219, 24
- O'Connor, E., & Ott, C. D. 2010, Classical and Quantum Gravity, 27, 114103
- . 2011, The Astrophysical Journal, 730, 70
- . 2013, The Astrophysical Journal, 762, 126
- Oda, T., Hino, M., Muto, K., Takahara, M., & Sato, K. 1994, Atomic Data and Nuclear Data Tables, 56, 231
- Paar, N., Colò, G., Khan, E., & Vretenar, D. 2009, Phys. Rev. C, 80, 055801
- Poves, A., Sanchez-Solano, J., Caurier, E., & Nowacki, F. 2001, Nuclear Physics A, 694, 157
- Schatz, H., Gupta, S., Möller, P., et al. 2014, Nature, 505, 62
- Scott, M., Shimbara, Y., Austin, S. M., et al. 2014, Physical Review C, 90, 025801
- Steffen, M. 1990, A&A, 239, 443
- Steiner, A. W., Hempel, M., & Fischer, T. 2013, The Astrophysical Journal, 774, 17
- Toki, H., Hirata, D., Sugahara, Y., Sumiyoshi, K., & Tanihata, I. 1995, Nuclear Physics A, 588, c357
- Typel, S., Röpke, G., Klähn, T., Blaschke, D., & Wolter, H. H. 2010, Physical Review C, 81, 015803
- Woosley, S., & Heger, A. 2007, Physics Reports, 442, 269
- Woosley, S. E., & Weaver, T. A. 1995, The Astrophysical Journal Supplement Series, 101, 181
- Wu, C. F. J. 1986, The Annals of Statistics, 14, 1261